



HHS Public Access

Author manuscript

Neuroimage. Author manuscript; available in PMC 2017 November 15.

Published in final edited form as:

Neuroimage. 2016 November 15; 142: 381–393. doi:10.1016/j.neuroimage.2016.08.022.

Fast imaging of mean, axial and radial diffusion kurtosis

Brian Hansen¹, Noam Shemesh², and Sune Nørhøj Jespersen^{1,3,*}

¹Center of Functionally Integrative Neuroscience (CFIN) and MINDLab, Clinical Institute, Aarhus University, Aarhus, Denmark

²Champalimaud Neuroscience Programme, Champalimaud Centre for the Unknown, Lisbon, Portugal

³Department of Physics and Astronomy, Aarhus University, Aarhus, Denmark

Abstract

Diffusion kurtosis imaging (DKI) is being increasingly reported to provide sensitive biomarkers of subtle changes in tissue microstructure. However, DKI also imposes larger data requirements than diffusion tensor imaging (DTI), hence, the widespread adaptation and exploration of DKI would benefit from more efficient acquisition and computational methods. To meet this demand, we recently developed a method capable of estimating mean kurtosis with only 13 diffusion weighted images. This approach was later shown to provide very accurate mean kurtosis estimates and to be more efficient in terms of contrast to noise per unit time. However, insofar, the computation of two other critical DKI parameters, radial and axial kurtosis, has required the estimation of all 22 variables parameterizing the full DKI signal expression. Here, we present two strategies for estimating all of DKI's principal parameters – mean kurtosis, radial kurtosis, and axial kurtosis – using only 19 diffusion weighted images, compared to the current state-of-the-art acquisitions typically requiring about 60 images. The first approach is based on axially symmetric diffusion and kurtosis tensors, presented here for the first time, and referred to as axially symmetric DKI. The second approach is applicable in tissues with a priori known principal diffusion direction, and does not require fitting of any kind. The approaches are evaluated in human brain in vivo as well as in fixed rat spinal cord, and are demonstrated to provide metrics in good agreement with their full DKI counterparts estimated with nonlinear least squares. For small data sets and in white matter, axially symmetric DKI provides more accurate and robust estimates than unconstrained DKI. The significant acceleration achieved further paves the way to routine application of the technique.

*Corresponding Author: Sune Jespersen, CFIN / Dept. of Physics and Astronomy, Aarhus University, Building 10G, 5th Floor, Nørrebrogade 44, DK-8000 Århus C, Denmark, Phone/ +4578463334 / sune@cfin.au.dk.

²If accepted

Publisher's Disclaimer: This is a PDF file of an unedited manuscript that has been accepted for publication. As a service to our customers we are providing this early version of the manuscript. The manuscript will undergo copyediting, typesetting, and review of the resulting proof before it is published in its final citable form. Please note that during the production process errors may be discovered which could affect the content, and all legal disclaimers that apply to the journal pertain.

Introduction

Diffusion kurtosis imaging (Jensen and Helpert, 2010; Jensen et al., 2005) continues to attract increasing interest, due to its potential sensitivity to tissue microstructural properties not captured by the diffusion tensor. Parameters derived from the diffusion kurtosis tensor have been shown to provide complementary information to those based on the diffusion tensor in several studies. In stroke for example, kurtosis based parameters improve the detection of tissue changes (Rudrapatna et al., 2014), and mean kurtosis remains elevated after mean diffusivity normalizes (Weber et al., 2015). In demyelinating diseases such as multiple sclerosis, kurtosis derived parameters are associated with cognitive deficits (Bester et al., 2015) and detect cortical alterations, whereas DTI parameters are not (or could not be detected) (Guglielmetti et al., 2016). Similar benefits of DKI have been reported in mild traumatic brain injury e.g. in (Grossman et al., 2012), see also review of DKI in this context in (Ostergaard et al., 2014). DKI has an increased number of parameters compared to DTI (22 versus 7), and hence, the estimation of DKI metrics requires substantially more data. A traditional DKI acquisition samples 30 directions at 5 b-shells (Poot et al., 2010), although more modest protocols with 30 directions at two non-zero b-values can also provide satisfactory estimation quality (Fieremans et al., 2011). While important for research, such lengthy MRI protocols are an obstacle for clinical adaptation, where time is often limited, especially when the practical clinical utility of DKI is not yet fully validated. This imposes a significant constraint towards routine implementation of DKI, as well as its testing in different clinical scenarios. We recently proposed a fast imaging framework, capable of estimating mean kurtosis on the basis of only 13 (139 protocol (Hansen et al., 2013a)) or 19 (199 protocol (Hansen et al., 2015)) diffusion weighted images. In contrast to other methods suggested to accelerate DKI by reducing the data requirements (Giannelli and Toschi, 2016; Golkov et al., 2015; Tachibana et al., 2015), our approach does not rely on additional assumptions or approximations beyond the few already inherent to DKI. Our approach was later adopted and validated in a rat model of stroke (Sun et al., 2014), and applied in human cancer patients, where it was shown to discriminate among different brain tumor types (Tietze et al., 2015). Very recently, the 139 fast DKI protocol was shown to afford higher contrast to noise ratio per unit time compared to a routine DKI protocol (Wu et al., 2016b).

While the 139/199 schemes have enabled a substantial acceleration for mean kurtosis imaging with very high parameter fidelity comparable to standard estimation methods (Hansen et al., 2015), it has not previously allowed estimation of axial and radial kurtosis values. Indeed, the most general DKI signal involves 22 parameters, which cannot all be determined in the absence of prior knowledge with only 19 measurements. Although published studies have identified mean kurtosis as a kurtosis parameter that can be sufficiently sensitive to provide contrast in disease, some also report differences in axial and radial kurtosis (Conklin et al., 2016; Guglielmetti et al., 2016; Kelm et al., 2016; Nie et al., 2015). Moreover, in highly directional tissues, such as e.g. spinal cord (Cheung et al., 2008; Hui et al., 2008b), changes in mean kurtosis are more difficult to interpret, as they combine properties across directions that are expected to behave quite differently. This incentivizes the development of accelerated DKI acquisition and analysis schemes, capable of extracting these salient DKI driven metrics.

Here we propose and evaluate two new approaches to measure axial and radial kurtosis, in addition to mean kurtosis, using the 199 protocol. The first approach for fast estimation of axial and radial kurtosis works by approximating the diffusion signal using axially symmetric diffusion and kurtosis tensors. This reduces the total number of DKI parameters to only 8, and it is therefore possible to determine them all by nonlinear fitting to the 19 measurements acquired with the 199 protocol. Axial symmetry is likely to be a reasonable approximation in certain types of tissues, such as in major white matter fiber bundles in the brain, as well as in the spinal cord and peripheral nerves. The second approach does not require fitting and does not assume axial symmetry, but necessitates a priori knowledge of the principal axis of the diffusion tensor. This makes the approach best suited for certain applications, e.g. spinal cord or peripheral nerve imaging. Here we illustrate both approaches with diffusion weighted imaging of the human brain, as well as the rat spinal cord, and compare the performance of the two approaches to each other, and to conventional DKI metrics. We also provide freely available code allowing interested researchers and clinicians to analyze DKI data with our methods.

Theory

The basic equation of DKI signals reads

$$\begin{aligned} \log S(b, \hat{n}) &= -bn_i n_j D_{ij} + \frac{1}{6} b^2 \bar{D}^2 n_i n_j n_k n_l W_{ijkl} = -bD(\hat{n}) + \frac{1}{6} b^2 \bar{D}^2 W(\hat{n}) \\ &= -bD(\hat{n}) + \frac{1}{6} b^2 D(\hat{n})^2 K(\hat{n}) \end{aligned} \quad (1)$$

where b is the diffusion weighting applied along $\hat{n} = (n_x, n_y, n_z)$, D is the diffusion tensor, and subscripts label Cartesian components (e.g. $i = x, y, z$). The kurtosis tensor W and the apparent excess kurtosis $K(\hat{n})$ are defined as in (Jensen et al., 2005). On this basis it was shown that the mean (of the) kurtosis tensor, \bar{W} or MKT, being defined as the directionally averaged observed kurtosis

$$\bar{W} \equiv \frac{1}{4\pi} \int_{S_2} d\hat{n} W(\hat{n}) \quad (2)$$

over the sphere S_2 , may be obtained from $W(\hat{n})$ along nine distinct directions, $\hat{n}^{(i)}$, $\hat{n}^{(i+)}$ and $\hat{n}^{(i-)}$ ($i=1,2,3$) (Hansen et al., 2014a; Hansen et al., 2015; Hansen et al., 2014b), defined in Table 1. This was shown to follow from the identity

$$\frac{1}{15} \left(\sum_{i=1}^3 \log S(b, \hat{n}^{(i)}) + 2 \sum_{i=1}^3 \log S(b, \hat{n}^{(i+)}) + 2 \sum_{i=1}^3 \log S(b, \hat{n}^{(i-)}) \right) = -b\bar{D} + \frac{1}{6} b^2 \bar{D}^2 \bar{W} \quad (3)$$

A protocol acquiring one $b=0$ image and all nine directions in Table 1 at two b -values, b_1 and b_2 (hence we refer to this as the 199 protocol (Hansen et al., 2015)), allows one to use Eq. (3) to form a set of two equations with two unknowns \bar{D} and \bar{W} :

$$\begin{aligned} A_1 &\equiv \frac{1}{15} \left(\sum_{i=1}^3 \log S(b_1, \hat{n}^{(i)}) + 2 \sum_{i=1}^3 \log S(b_1, \hat{n}^{(i+)}) + 2 \sum_{i=1}^3 \log S(b_1, \hat{n}^{(i-)}) \right) = -b_1 \bar{D} + \frac{1}{6} b_1^2 \bar{D}^2 \bar{W} \\ A_2 &\equiv \frac{1}{15} \left(\sum_{i=1}^3 \log S(b_2, \hat{n}^{(i)}) + 2 \sum_{i=1}^3 \log S(b_2, \hat{n}^{(i+)}) + 2 \sum_{i=1}^3 \log S(b_2, \hat{n}^{(i-)}) \right) = -b_2 \bar{D} + \frac{1}{6} b_2^2 \bar{D}^2 \bar{W} \end{aligned} \quad (4)$$

and solve to obtain estimates for \bar{D} :

$$\bar{D} = (b_1^2 A_2 - b_2^2 A_1) / (b_1 b_2^2 - b_2 b_1^2) \quad (5)$$

and for \bar{W} :

$$\bar{W} = 6b_1 b_2 (A_1 b_2 - A_2 b_1) (b_1 - b_2) / (A_1 b_2^2 - A_2 b_1^2)^2 \quad (6)$$

Note that a similar procedure cannot be applied to the estimation of conventional mean kurtosis (MK or \bar{K}) (Jensen et al., 2005), because of the multiplication with $D(\hat{n})$ in Eq. (1).

Axial K_{\parallel} and radial K_{\perp} kurtosis were originally defined by Hui and colleagues (Hui et al., 2008a, b) in terms of the apparent kurtosis $K(\hat{n})$ along the direction of the diffusion tensor eigenvectors, \mathbf{v}_1 , \mathbf{v}_2 and \mathbf{v}_3 in order of decreasing diffusivities λ_1 , λ_2 and λ_3 as

$$\begin{aligned} K_{\parallel} &= K(\mathbf{v}_1) = (\bar{D}^2 / \lambda_1^2) W_{zzzz} \\ K_{\perp} &= \frac{K(\mathbf{v}_2) + K(\mathbf{v}_3)}{2} = \frac{\bar{D}^2}{2} (W_{xxxx} / \lambda_2^2 + W_{yyyy} / \lambda_3^2) \end{aligned} \quad (7)$$

The latter equalities apply in the principal coordinate system in which \mathbf{v}_1 , \mathbf{v}_2 and \mathbf{v}_3 are parallel to the z, y and x axes, respectively. A so far unreported effect of the original radial kurtosis in Eq. (7), is that it is not rotationally invariant. Fundamentally, this is related to its definition in terms of the eigenvectors of D , because W does not necessarily share its symmetry. For example, in cases where D is approximately axially symmetric, e.g. in regions with fiber bundles crossing at close to right angles, the two minor diffusion tensor eigenvalues are approximately degenerate, and hence the associated eigenvectors can be any pair of perpendicular vectors in the transverse plane. In such a case, they are effectively determined by fitting algorithm, initialization, and noise. However, W (as well as $K(\hat{n})$) need not possess this symmetry, and as a result, radial kurtosis is not uniquely defined. In regions where D is isotropic (e.g. gray matter or where three fiber bundles cross at right

angles) the primary eigenvector direction will also be effectively random and hence both directional kurtosis metrics are poor reporters of underlying fiber architecture.

A more recent definition of radial kurtosis was proposed independently by Poot et al. (Poot et al., 2010) and Jensen et al. (Jensen and Helpert, 2010), as the average apparent kurtosis perpendicular to the principal diffusion eigenvector, i.e.

$$K_{\perp} \equiv \frac{1}{2\pi} \int_{S_1} d\hat{n} K(\hat{n}) = \frac{1}{2\pi} \int_0^{2\pi} d\varphi K(\mathbf{v}_2 \cos\varphi + \mathbf{v}_3 \sin\varphi) \quad (8)$$

This definition has since become standard, and we henceforth refer to it as the conventional radial kurtosis. In the principal coordinate system defined earlier, K_{\perp} can be expressed in terms of elements of the kurtosis tensor and diffusion tensor eigenvalues as (Tabesh et al., 2011):

$$K_{\perp} = G_1(\lambda_1, \lambda_2, \lambda_3) W_{xxxx} + G_1(\lambda_1, \lambda_3, \lambda_2) W_{yyyy} + G_2(\lambda_1, \lambda_2, \lambda_3) W_{xxyy} \quad (9)$$

where

$$G_1(\lambda_1, \lambda_2, \lambda_3) = \frac{(\lambda_1 + \lambda_2 + \lambda_3)^2}{18\lambda_2(\lambda_2 - \lambda_3)^2} \left(2\lambda_2 + \frac{\lambda_3^2 - 3\lambda_2\lambda_3}{\sqrt{\lambda_2\lambda_3}} \right)$$

$$G_2(\lambda_1, \lambda_2, \lambda_3) = \frac{(\lambda_1 + \lambda_2 + \lambda_3)^2}{3(\lambda_2 - \lambda_3)^2} \left(\frac{\lambda_2 + \lambda_3}{\sqrt{\lambda_2\lambda_3}} - 2 \right) \quad (10)$$

In order to enable direct estimation of directional kurtosis metrics from a few diffusion directions, we use the mathematically more convenient kurtosis tensor $W(\hat{n})$ instead of the apparent kurtosis $K(\hat{n})$ to define axial and radial tensor kurtosis. Thus, axial tensor kurtosis W_{\parallel} is the apparent tensor kurtosis along the primary eigenvector \mathbf{v}_1 of the diffusion tensor. In the principal coordinate frame of the diffusion eigenvector, where $\hat{z} = \mathbf{v}_1$, $\hat{y} = \mathbf{v}_2$, and $\hat{x} = \mathbf{v}_3$,

$$W_{\parallel} = W(\mathbf{v}_1) = W_{zzzz} \quad (11)$$

We define the radial tensor kurtosis W_{\perp} similarly to Eq. (8) by averaging $W(\hat{n})$ over the circle S_1 perpendicular to the axis of symmetry, i.e. the equator associated with the primary eigenvector:

$$W_{\perp} \equiv \frac{1}{2\pi} \int_{S_1} d\hat{n} W(\hat{n}) = \frac{3}{8} (W_{xxxx} + W_{yyyy} + 2W_{xxyy}) \quad (12)$$

The latter identity holds as long as $\mathbf{v}_1 = \hat{z}$, and does not depend on the choice of x and y axes. Importantly, in contrast to the original radial kurtosis in Eq. (7), our radial tensor

kurtosis does not only involve kurtosis along the two axes, but also a cross term W_{xxyy} . Notably, both definitions of radial kurtosis in Eqs. (8) and (12) are rotationally invariant in the case of degenerate minor eigenvalues of the diffusion tensor, and hence do not suffer the problem with the original radial kurtosis described earlier.

Using the definition $W(\hat{n}) = n_i n_j n_k n_l W_{ijkl}$, it is straightforward to verify that radial tensor kurtosis can be computed from the kurtosis along 4 directions perpendicular to \hat{z} , for example:

$$\begin{aligned} W_{\perp} &= \frac{3}{8}(W_{xxxx} + W_{yyyy} + 2W_{xxyy}) \\ &= \frac{1}{4} \left(W(\hat{x}) + W(\hat{y}) + W\left(\frac{\hat{x} + \hat{y}}{\sqrt{2}}\right) + W\left(\frac{\hat{x} - \hat{y}}{\sqrt{2}}\right) \right) \end{aligned} \quad (13)$$

where \hat{x} and \hat{y} may be any perpendicular directions in the plane orthogonal to the principal diffusion tensor eigenvector. Specifically, we may choose $\hat{y} = \mathbf{v}_2$, and $\hat{x} = \mathbf{v}_3$. This expression reveals an advantage of the tensor based definition radial kurtosis in that it allows the new radial kurtosis to be directly evaluated from the kurtosis along four directions. This property is rooted in the order four nature of the kurtosis tensor. An expression somewhat similar to Eq. (12) can be found for K_{\perp} in (Jensen and Helpert, 2010; Tabesh et al., 2011) which, however, requires the diffusion tensor eigenvalues to be known, which is not the case in Eq. (12). We will take advantage of this property of the radial tensor kurtosis in the direct estimation scheme for systems with known principal axis to be discussed below.

A somewhat peculiar side effect of working with W , is the property that its value $W(\hat{n})$ along any direction \hat{n} is affected by the diffusion signal in other directions due to the multiplication of mean diffusivity in Eq. (1): however, this may easily be avoided if desired, by considering instead the tensor $W\overline{D}^2$. In a similar vein, we note that for the comparison of the degree of non-gaussianity along the radial and axial directions, it is natural to consider for each direction separately the relative size of the second term in the cumulant expansion to that of the first term squared. Hence, a rescaling of the axial and radial tensor kurtosis is convenient, and therefore we define

$$\begin{aligned} K_{\parallel} &= W_{\parallel} \overline{D}^2 / D_{\parallel}^2 \\ K_{\perp} &= W_{\perp} \overline{D}^2 / D_{\perp}^2 \end{aligned} \quad (14)$$

This also removes the influence of the diffusion signal along other directions from the metrics. Note that this definition of axial kurtosis is equivalent to the conventional one Eq. (7), whereas the radial kurtosis in Eq. (14) in general is different from that of Eq. (8). When there is risk of ambiguity we refer to the Jensen/Poot definitions as K_{\parallel}^{JP} and K_{\perp}^{JP} .

Even though we here mainly employ the definitions in Eq. (14), we stress that the methods introduced below can also be used to extract directional kurtosis metrics defined in the conventional way (Jensen and Helpert, 2010; Poot et al., 2010; Tabesh et al., 2011). Matlab code to extract all these metrics is available at <http://cfin.au.dk/cfinmindlab-labs-research->

groups/neurophysics/software¹. While the two definitions of radial kurtosis reflect similar physical properties, our preference for working with the present definition of radial kurtosis (Eq. (14)) over the conventional (Eq. (8)) include the following differences: 1) It is mathematically simpler than the conventional, compare Eqs. (9) and (10) with Eq. (12). 2) It does not necessitate eigenvalue decomposition of the diffusion tensor. In fact, the latter property enables estimation of radial kurtosis from 4 diffusion directions without fitting, as we shall see below, whereas to obtain the conventional radial kurtosis, it is necessary to apply either fitting or an additional assumption of axial symmetry.

In the following, we will experimentally examine properties of radial (K_{\perp}) and axial (K_{\parallel}) kurtosis and how they can be determined rapidly with the fast kurtosis imaging protocol (199) proposed in Refs. (Hansen et al., 2013a; Hansen et al., 2014a; Hansen et al., 2015). First however, we present the theoretical backgrounds of the two methods.

Kurtosis for axially symmetric systems: axially symmetric DKI

In general, the kurtosis tensor has 15 independent parameters assuming full permutation symmetry of its indices (Jensen and Helpert, 2010; Jensen et al., 2005). In a system with axial symmetry (taking the z -axis to be parallel to the axis of symmetry), the kurtosis is characterized by three independent parameters, for example \bar{W} (mean kurtosis), K_{\parallel} (axial kurtosis, z -axis) and K_{\perp} (radial kurtosis, xy -plane). This can be seen for example by considering the Laplace expansion of $W(\hat{n})$: Since it is a quartic form in \hat{n} , the Laplace expansion involves only spherical harmonics Y_{lm} up to order $l=4$. Furthermore, due to antipodal symmetry, only even l terms appear, and the azimuthal symmetry further selects only the $m=0$ zonal spherical harmonics. This leaves only the three real coefficients of Y_{00} , Y_{20} and Y_{40} to be specified. The axis of symmetry must be specified as well, leaving a total of only 5 degrees of freedom for an axially symmetric kurtosis tensor. In contrast to the diffusion tensor, the mean kurtosis is independent of the radial and axial kurtosis, which also applies to the earlier definitions (Hui et al., 2008a, b) (Jensen and Helpert, 2010; Poot et al., 2010; Tabesh et al., 2011). The reason for this has to do with the property that apparent kurtosis evaluated along a direction in the yz -plane, e.g., involves cross terms such as W_{yyzz} which do not appear in radial nor axial kurtosis. Importantly, we note that the conventional and present definitions of radial kurtosis coincide for axially symmetric systems.

In an axially symmetric system, with the z -axis chosen to be parallel to the axis of symmetry, the kurtosis along an arbitrary direction characterized by a polar angle θ is then:

$$W(\theta) = \frac{1}{16} \left(\cos(4\theta)(10W_{\perp} + 5W_{\parallel} - 15\bar{W}) + 8\cos(2\theta)(W_{\parallel} - W_{\perp}) - 2W_{\perp} + 3W_{\parallel} + 15\bar{W} \right) \quad (15)$$

Similarly for $D(\theta)$

¹If accepted

$$D(\theta) = D_{\perp} + \cos^2(\theta)(D_{\parallel} - D_{\perp}) \quad (16)$$

This can be straightforwardly verified by computing the mean, axial, and radial kurtosis from Eq. (15) using their definitions in Eqs. (2), (11) and (12). Note that in axially symmetric systems, the present definitions of both radial and axial kurtosis are identical to the conventional definitions. If the direction of diffusion weighting is not well defined, such as when cross terms from imaging gradients are significant, it is necessary to have explicit and coordinate independent tensor forms:

$$W = \frac{1}{2}(10W_{\perp} + 5W_{\parallel} - 15\overline{W})P + W_{\perp} + \frac{3}{2}(5\overline{W} - W_{\parallel} - 4W_{\perp})Q \quad (17)$$

$$D = D_{\perp}I + (D_{\parallel} - D_{\perp})\mathbf{u}\mathbf{u}^T \quad (18)$$

where I in Eq. (18) is the identity matrix and \mathbf{u} is a unit vector along the axis of symmetry. The tensors P , \mathbb{I} and Q are defined as

$$P_{ijkl} = u_i u_j u_k u_l$$

$$Q_{ijkl} = \frac{1}{6}(u_i u_j \delta_{kl} + u_i u_k \delta_{jl} + u_i u_l \delta_{jk} + u_j u_k \delta_{il} + u_j u_l \delta_{ik} + u_k u_l \delta_{ij})$$

$$\mathbb{I}_{ijkl} = \frac{1}{3}(\delta_{ij} \delta_{kl} + \delta_{ik} \delta_{jl} + \delta_{il} \delta_{jk}) \quad (19)$$

This allows contraction of the tensors with the appropriate b-matrices, as needed for computing the signal, cf. Eq. (1):

$$b_{ij} b_{kl} W_{ijkl} = \frac{1}{2}(10W_{\perp} + 5W_{\parallel} - 15\overline{W})(\mathbf{u}^T \mathbf{b} \mathbf{u})^2 + \frac{1}{2}(5\overline{W} - W_{\parallel} - 4W_{\perp})(\mathbf{u}^T \mathbf{b} \mathbf{u} \text{Tr}(\mathbf{b}) + 2\mathbf{u}^T \mathbf{b} \mathbf{b} \mathbf{u}) + \frac{W_{\perp}}{3}(\text{Tr}(\mathbf{b})^2 + 2\text{Tr}(\mathbf{b} \otimes \mathbf{b})) \quad (20)$$

$$b_{ij} D_{ij} = \text{Tr}(\mathbf{b})D_{\perp} + (D_{\parallel} - D_{\perp})\mathbf{u}^T \mathbf{b} \mathbf{u} \quad (21)$$

Here $\text{Tr}(\mathbf{b})$ is the trace of the matrix \mathbf{b} , and we use \otimes to denote the tensor product; e.g. for two second order tensors \mathbf{A} and \mathbf{B} , the tensor product $\mathbf{A} \otimes \mathbf{B}$ is an order four tensor with Cartesian components $(\mathbf{A} \otimes \mathbf{B})_{ijkl} = A_{ij} B_{kl}$.

In the following, we analyze human brain and rat spinal cord diffusion MRI data using the assumption of axially symmetric tensors — i.e., axially symmetric DKI with only 8

parameters. The idea is that using the 199-scheme allows us to fit the 19 signals to Eq. (1), enabling a fast determination of the 8 unknown parameters fully characterizing the DKI signal.

Axial and Radial Kurtosis for systems with known principal axis: direct 199 approach

For this approach, we assume the principal axis to be known in advance, and define it to be the z-axis. Then axial and radial kurtosis can be rapidly estimated from five of the directions already included in our 199 design. On the basis of Eqs. (1) and (13) it can be straightforwardly worked out that

$$\frac{1}{4}(\log(S(b_i, \hat{n}^{(1)})) + \log(S(b_i, \hat{n}^{(2)})) + \log(S(b_i, \hat{n}^{(3+)}) + \log(S(b_i, \hat{n}^{(3-)})) = -b_i D_{\perp} + \frac{1}{6} b_i^2 \bar{D}^2 W_{\perp} \equiv A_i, \quad (22)$$

analogously to Eq. (4), but note that A_i is not the same in the two equations. Acquiring this at two shells (with b-values b_1 and b_2), we can solve for radial diffusivity defined in the standard way

$$D_{\perp} = \frac{A_2 b_1^2 - A_1 b_2^2}{b_1 b_2 (b_2 - b_1)} \quad (23)$$

and radial tensor kurtosis

$$W_{\perp} \bar{D}^2 = \frac{6}{b_1 b_2} \frac{A_2 b_1 - A_1 b_2}{(b_2 - b_1)} \quad (24)$$

Mean diffusivity \bar{D} is estimated from the same data using the procedure outlined in detail in (Hansen et al., 2013a; Hansen et al., 2015). The axial kurtosis can be estimated quite simply from measurements at two b-values along the axial direction, i.e. $\hat{n}^{(3)}$. With this procedure, no fitting is involved to obtain any of the metrics \bar{W} , K_{\perp} and K_{\parallel} as well as analogous diffusion tensor metrics, and even the full diffusion tensor (Hansen et al., 2015) can be obtained with fitting. This means that the conventional radial and axial kurtoses, which require all three diffusion tensor eigenvalues for their calculation, can also be estimated with this method using the theory in (Tabesh et al., 2011). All of the above assumes that the axis of symmetry is known in advance, such that the scheme can be applied with one of the axes aligned with it (here the z-axis). Below, we test this approach in rat spinal cord, where the primary diffusion eigenvector in the spinal cord's white matter is assumed to be along the spinal cord longitudinal axis, as clearly demonstrated in (Flint et al., 2010; Hansen et al., 2011).

Methods

Human data was acquired in a normal volunteer on a Siemens Trio 3T using a 32 channel head coil and a double spin echo DW EPI sequence with cerebrospinal fluid (CSF) suppression by inversion recovery as per (Jones et al., 2013). Padding was used to avoid head motion during the acquisitions. Image resolution was 3 mm isotropic with an SNR of 39 at $b=0$. Throughout SNR was calculated as the average of a homogenous signal region divided by the standard deviation of the signal in a background region, corrected for Rayleigh distribution in a standard manner. A total of 19 slices were acquired, with $TR=4300$ ms, $TE=103$ ms. Data consisted of one $b=0$ image and 14 shells with 33 directions at b -values of $0.2\text{--}3.0$ $\text{ms}/\mu\text{m}^2$. The 33 directions were chosen from a 3 dimensional 24 point spherical 7-design (Hardin and Sloane, 1996), appended with the 9 directions (Table 1) identified previously (Hansen et al., 2013a). Human data was acquired by permission from the local ethics committee and informed consent was obtained prior to acquisition.

Data from rat spinal cord was acquired using an ultrahigh-field 16.4T Bruker Aeon Ascend magnet (700MHz proton frequency) equipped with gradients capable of producing up to 3000mT/m in every direction (MICRO5 micro-imaging gradients, Bruker Biospin, Ettlingen, Germany). All animal handling was done in accordance with EU directive 2010/63/EU for animal experiments, and approved in advance by the Champalimaud Centre for the Unknown's animal ethics committee. A Long-Evans rat, 14–16 weeks old, was perfused with 4% PFA and the cervical spinal cord (SC) was isolated, washed in PBS, placed in a 5mm NMR tube and placed in the magnet with its length axis aligned with the main magnetic field. Diffusion weighted imaging (with echo-planar readout) with $TR/TE = 4000/35$ ms and 4 averages was performed with in-plane resolution of 36×36 μm^2 and a slice thickness of 1 mm using axial slice orientation and 70% k -space coverage for acceleration. SNR at $b=0$ was larger than 60. Diffusion times (δ) were 10ms/2ms, and diffusion gradients sampled the same directions as for the human brain data set but with 9 nonzero b -values having nominal values linearly interspersed between 0.6 $\text{ms}/\mu\text{m}^2$ and 5.4 $\text{ms}/\mu\text{m}^2$. 10 $b=0$ images were acquired.

Postprocessing

All data sets were evaluated visually for quality (artifacts, subject/sample movement, and field drift). Due to the padding around the subject's head, image registration was found to be unnecessary. This was also the case for the rat spinal cord sample held in the NMR tube. To reduce the impact of Gibbs ringing, smoothing with a two-dimensional Gaussian filter (FWHM 1.75 x voxel size) was applied to the human in vivo data set (Tabesh et al., 2011). Nonlinear least squares fitting was applied with Levenberg–Marquardt algorithm implemented in Matlab® (Natick, Massachusetts). In the case of fitting to the axially symmetric DKI model, we found that a good starting guess for the axis of symmetry was crucial. Here, we used the primary diffusion eigenvector of the diffusion tensor, which can also be estimated from the 199 data sets. The axially symmetric DKI representation was applied both to the full data sets, and to subsets corresponding to the 199 protocol. For the human data set, the 199 data set was selected from the $b=1.0$ $\text{ms}/\mu\text{m}^2$ and $b=2.6$ $\text{ms}/\mu\text{m}^2$ shells, whereas for the rat spinal cord $b=1.3$ $\text{ms}/\mu\text{m}^2$ and $b=5.5$ $\text{ms}/\mu\text{m}^2$ were used, mainly

due to the lower temperature in the magnet bore which renders the intrinsic diffusion processes slower compared to those in the living human brain. The direct 199 approach applicable in tissues with known primary diffusion direction was applied to the rat spinal cord data with b-values of $1.9 \text{ ms}/\mu\text{m}^2$ and $5.5 \text{ ms}/\mu\text{m}^2$. For the evaluation of direct 199 performance in rat spinal cord, gray and white matter was segmented manually on an FA map based on known spinal cord anatomy.

Results

Figure 1 compares (from left to right) the proposed radial K_{\perp} and axial K_{\parallel} kurtosis and MKT (i.e. \bar{W}) (top row) to the conventionally defined counterparts (middle row) in human brain. Radial and axial diffusivities, along with FA, are also shown for comparison (left to right, bottom row). The diffusivities are given in units of $\mu\text{m}^2/\text{ms}$. MKT and MK appear quite similar, as also noticed previously (Glenn et al., 2015; Hansen et al., 2013a; Hansen et al., 2014a; Hansen et al., 2014b; Sun et al., 2014). The overall contrast in the two radial kurtosis maps likewise appears qualitatively similar, and both appear somewhat FA weighted. Nevertheless, conventional K_{\perp} has higher numerical values in white matter than K_{\perp} . The two maps of axial kurtosis K_{\parallel} are identical by construction.

The difference between the Jensen/Poot definition and our K_{\perp} is examined in more detail in Fig. 2, which shows a map of their relative difference and the corresponding histogram. It is clear that the largest differences occur mostly in white matter, though some cortical areas show some slight differences as well. While the histogram is sharply peaked around zero, it also reveals a fat tail of voxels with K_{\perp}^{JP} larger than K_{\perp} with up to 100%.

Axially symmetric DKI

Figure 3 is also based on the human brain data and compares the K_{\perp} , K_{\parallel} , and MKT (left to right) estimates from axially symmetric DKI to those obtained from the fits to general DKI (top row). The axially symmetric model estimates were obtained in two ways: fitting the axially symmetric DKI to the full data set (middle row) and to a 199 subset of the data (bottom row). The agreement between the maps based on axially symmetric DKI and those based on unconstrained DKI is striking, and one has to scrutinize the maps to detect differences. The reduced data set is unsurprisingly seen to produce noisier maps, but the contrast remains quite similar.

A more detailed comparison is illustrated in Fig. 4 with scatterplots (human white matter, 22 slices) between general DKI and axial DKI for each parameter (top row), and between axial DKI and axial DKI analysed with 199 subsampled data (bottom row). The best fit straight line is added, and points are color coded according to 6 levels of FA. Mean kurtosis is very well reproduced with the axial assumption, and displays a correlation coefficient of 0.996 to that obtained from conventional DKI. Here, and in the following, all reported correlation coefficients are Pearson's correlation coefficients. Radial and especially axial kurtosis show a bit more scatter, but with correlation coefficients of 0.99 and 0.95, respectively. Upon reducing the data to the 199 subset, more scatter in all the three metrics is observed, with axial kurtosis again showing the poorest correspondence. Moreover, the best fit straight lines deviate more from the identity. For both the full and 199 data sets, better agreement is found

in the higher FA regions, and this tendency is especially pronounced for axial and radial kurtosis and in the reduced data set. Nevertheless, a strong linear correlation remains, with correlation coefficients of 0.78, 0.58, and 0.90 for radial, axial and MKT respectively.

The reason for the good overall agreement in Fig. 4, is not necessarily that the DKI signal is axially symmetric in all brain voxels. In Fig. 5, the radial variability of the kurtosis $W(\hat{n})$ is investigated through the difference $\alpha = (W_{\max} - W_{\min})/W_{\perp}$ between the maximum and minimum kurtosis values in radial directions, relative to the mean (i.e. radial tensor kurtosis W_{\perp}). The histograms in Fig. 5a show the distribution of α for the full DKI fitted to actual data (blue) and to data synthesized from the axially symmetric fit (orange). The fits were based on equal data amounts and noise was added to the synthetic signal to match the experimental SNR = 39 at b=0). Maps are provided in panels b and c where it can be seen that while α is typically on the order of 10%, it approaches 100% in several voxels, and in particular is much larger for real data (panel b) than the same quantity computed from artificial data generated directly from the previously estimated axially symmetric tensors, and refitted to the full DKI signal (panel c). Finally, an F-test comparing the goodness of fit of full and axially symmetric DKI to the complete data set favors the full representation in the far majority of voxels (data not shown).

In a follow-up analysis, we compared the precision and accuracy of kurtosis metrics estimated with a standard protocol with $1 \times 30 \times 30$ directions at b=0, 1000 and 2600 ms/mm² from axially symmetric DKI and unconstrained DKI with simulated data (SNR=39) from a typical white matter and a typical gray matter voxel. Figure 6 shows histograms over 1000 noise repetitions, and indicates that axially symmetric DKI slightly outperforms unconstrained DKI in white matter, especially in terms of bias. The advantage of axially symmetric DKI further improves when the number of directions is decreased more. The histogram median and mid-95% range (distance between 2.5% and 97.5% quantiles) are provided in each graph.

Figure 7 is similar to Fig. 3, but for the spinal cord data. Here, radial and axial diffusivity and fractional anisotropy are also shown (top row) to demonstrate the different microstructural information conveyed by the kurtosis metrics. The remaining rows show K_{\perp} , K_{\parallel} , and MKT (left to right). Again, parameter maps based on the full data set (conventional DKI in second row and axially symmetric DKI in the third) are highly similar, whereas the 199 data set (bottom row) gives noisier maps of very similar contrast.

The scatterplots in Fig. 8 for all three kurtosis parameters shown in Fig. 7 demonstrate an excellent agreement between full tensor metrics and axially symmetric DKI metrics (top row): all correlation coefficients are above 0.99. For the metrics obtained by fitting to the 199 subset, correlations decreased to 0.94, 0.92, and 0.96 for radial, axial and MKT, respectively. Furthermore, axial kurtosis and mean kurtosis show a small propensity for underestimation.

Direct 199 approach

Next, we examine the 199 approach, which as described above is based on an a priori knowledge of the primary diffusion direction, here assumed to be the z-axis parallel to the

long axis of the spinal cord. Figure 9 (bottom row) shows the direct 199 estimate of the three kurtosis metrics (from left to right: K_{\perp} , K_{\parallel} , and \bar{W}) computed from the weighted sum of log signals Eqs. (24) and (6). The 199 estimates again display overall similar contrast to the measures obtained from fitting to the full data set (top row), although they clearly have more noise.

Finally, Fig. 10 is a scatterplot of the data corresponding to Fig. 9. The overall correlation between the two methods is 0.87, 0.88, and 0.94 for radial, axial and mean tensor kurtosis respectively. For radial kurtosis, the most scatter is seen in the white matter (blue points), in contrast to axial kurtosis which displays more scatter in gray matter (green).

Comparing estimates of D_{\perp} , D_{\parallel} , and FA from the three presented methods to conventional DKI in the rat spinal cord data the similarity of the maps is again striking with all correlations above 0.91 for D_{\perp} , 0.94 for D_{\parallel} , and 0.98 for FA (data not shown).

Discussion

In this paper, we evaluated two new methods to estimate radial and axial kurtosis from reduced diffusion weighted imaging data sets, to facilitate faster DKI, which in turn could enable a much broader range of applications of this important methodology. We have introduced a new definition of radial kurtosis, which differ from the earlier definitions in two ways. First, it was defined directly in terms of the more fundamental kurtosis tensor W , which is proportional to the fourth cumulant (Kiselev, 2011), as opposed to the apparent kurtosis $K(\hat{n})$ used by (Hui et al., 2008a, b) and later also for the definitions in (Jensen and Helpert, 2010; Poot et al., 2010), which coincide with the present definition in axially symmetric systems. Besides mathematical convenience, defining radial kurtosis directly in terms of the kurtosis tensor enables direct estimation of radial kurtosis from the diffusion signal along four directions without fitting, as shown here. This is analogous to the mean of the kurtosis tensor \bar{W} (or MKT) introduced in (Hansen et al., 2013a; Hansen et al., 2015), which has contrast very similar to traditional mean kurtosis (MK/ \bar{K}) (Jensen et al., 2005) as shown in (Glenn et al., 2015; Hansen et al., 2013a; Sun et al., 2014). This similarity was also observed here, as well as the similarity of conventional directional kurtosis metrics to the ones proposed here. The second way in which the new definitions differ applies only to the original definition of the radial kurtosis as the average apparent kurtosis along the two minor diffusion eigenvectors (Hui et al., 2008b). Instead, radial kurtosis was defined here via integration over the equator associated with the primary diffusion tensor eigenvector analogous to the conventional definitions (Jensen and Helpert, 2010; Poot et al., 2010). The originally proposed radial kurtosis does not fully reflect the values of apparent kurtosis in the perpendicular plane and results in a measure which is not rotationally invariant, for example in crossing fiber bundles where the diffusion tensor but not the kurtosis tensor is axially symmetric. In practice, it can render the radial apparent kurtosis noisier and less accurate than the radial tensor kurtosis. Strictly speaking, radial kurtosis as defined here or in (Jensen and Helpert, 2010; Poot et al., 2010) is not rotationally invariant either: if three identical fiber bundles of equal volume fractions were to cross at 90° , the diffusion tensor would be isotropic, but not the kurtosis tensor. Again, this would make radial and axial kurtosis depend on the arbitrary choice of diffusion tensor eigenvectors, which are

degenerate. However, we believe such a case to be very rare. Regions where such fiber arrangements exist may be identified by comparison of FA and Kurtosis Fractional anisotropy (KFA) (Hansen et al., 2013a; Jespersen, 2012) as recently demonstrated (Glenn et al., 2015; Hansen and Jespersen, 2016). Inspection of our human data seems to indicate that K_{\perp} is more stable than K_{\parallel} in such areas. To fully escape this problem, it seems necessary to rely only on kurtosis tensor properties when defining directional kurtosis metrics, but due to the order two nature of the kurtosis tensor eigenvectors (eigenmatrices), this is not straightforward (Qi et al., 2009; Qi et al., 2008).

Another potential issue with both definitions of radial and axial kurtosis so far, is their interpretation in regions with oblate tensors of axial symmetry, for example caused by the crossing of two fiber bundles at close to 90° . In such regions, the axis of symmetry is parallel to \mathbf{v}_3 and perpendicular to the plane of the fibers, whereas the principal diffusion direction \mathbf{v}_1 is in the plane. Hence, axial kurtosis is not evaluated along the diffusion tensor axis of symmetry, but some arbitrary direction \mathbf{v}_1 perpendicular to it, and the radial kurtosis mixes properties along the axis of symmetry with those perpendicular to it. One could potentially address this problem by using the third eigenvector in place of the first in all equations above, in cases when the diffusion tensor is estimated to be more oblate than prolate, as judged by some relevant criteria, e.g. $\lambda_1 - \lambda_2$ $\lambda_2 - \lambda_3$ (Westin et al., 2002). However, this results in rather noisy appearing maps (data not shown). Alternatively, fiber decomposition (Neto Henriques et al., 2015) could be used to compute the axial/radial kurtosis from a weighted sum of each of the fiber contributions, as the interpretation of radial and axial kurtoses is clearer in the case of individual fibers. Such a method would be computationally much more demanding.

One strategy to reduce the onerous data requirements for the estimation of radial and axial kurtosis is to reduce the total number of independent kurtosis tensor elements, for example by imposing axial symmetry as done here. While axial symmetry is a common approximation for the diffusion tensor, for example in microstructural modeling (Hansen et al., 2013b; Jespersen et al., 2010; Jespersen et al., 2007), axially symmetric diffusion kurtosis tensors have to our knowledge so far not been previously described. Explicit expressions for DKI with axially symmetric tensors were presented, reducing the total number of independent parameters to 8, which should be compared to general DKI with 22 parameters to be estimated. Corresponding Matlab scripts are freely available for usage, and can be downloaded at <http://cfin.au.dk/cfinmindlab-labs-research-groups/neurophysics/software>². Axially symmetric DKI signal expressions were then fit to human brain and rat spinal cord diffusion weighted images in order to provide estimates of \bar{W} , K_{\parallel} , and K_{\perp} . Perhaps somewhat surprisingly, all three metrics closely approximated the analogous metrics from fully general DKI in all regions of the brain.

To further investigate the reason behind this agreement, we asked whether diffusion and kurtosis tensors from DKI could in fact be axially symmetric, or approximately so, in the human brain. Maps and histograms of the radial variability (α in Fig. 5) of the apparent kurtosis revealed a relatively large dependence on direction, in particular there was much larger variability than from a signal generated with tensors having forced axial symmetry. This indicated that the radial variability was real, and not induced by noise or the fitting

procedure. Model comparisons with F tests further supported that the “ground truth” diffusion and kurtosis tensors are unlikely to be axially symmetric. Nevertheless, our results may indicate that the axially symmetric diffusion and kurtosis tensors which most closely approximate apparent diffusion and apparent kurtosis over all directions, have identical directional metrics to the underlying full diffusion and kurtosis tensors. Indeed, by using a spherical harmonics representation for the tensors, it is relatively straightforward to demonstrate that at least when the axis of symmetry is accurately estimated, the axially symmetric diffusion and kurtosis tensors that most closely approximate any given general diffusion and kurtosis tensors over all directions on the sphere, have the correct mean, axial, and radial diffusivities and kurtosis. Consistent with this, we showed that when the number of directions decreases, axially symmetric DKI provides more accurate and robust estimates of kurtosis metrics compared to unconstrained DKI, presumably due to the smaller number of parameters. For systems that do possess axial symmetry the radial kurtosis introduced here is identical to the conventional Poot/Jensen definition. Another advantage of axially symmetric DKI is its parameterization in terms of observable kurtosis metrics, which suggests an elegant and straightforward way to ensure nonnegative values of the apparent kurtosis over all directions. Rewriting Eq. (15) in terms of powers of cosine readily reveals necessary and sufficient conditions for the apparent kurtosis to be nonnegative to be $W_{\perp} > 0$, $W_{\parallel} > 0$ and $\overline{W} > (1/15)(8W_{\perp} + 3W_{\parallel} - 4\sqrt{W_{\perp}W_{\parallel}})$. In contrast, constraining the kurtosis to be nonnegative in the general case is nontrivial (Barmpoutis et al., 2009; Ghosh et al., 2014; Tabesh et al., 2011; Veraart et al., 2011). On the other hand, a drawback of axially symmetric DKI is that it does not lend itself to linear fitting, due to the inherently nonlinear parameterization.

When reducing the data to the 199 protocol, i.e. one $b=0$ image and nine directions on two b -shells, quite reasonable estimates of all three metrics could still be achieved, with correlations coefficients ranging from 0.70 to 0.94 to the metrics obtained from the full data set assuming axially symmetric DKI. Similar conclusions were drawn in spinal cord tissue, where axially symmetric DKI performed even better — in this case, all correlation coefficients exceeded 0.92. Presumably this can be at least partially ascribed to the simpler voxel composition at the resolution used to acquire the rat spinal cord data compared to human brain imaging, as well as the higher image quality and absence of physiological effects in ex vivo high field scanning. We note that that with only 8 free parameters, axially symmetric DKI allows estimation of all DKI metrics (regardless of definition) from small data sets. Here we use 199 data sets to show aspects of this, but it may be possible to efficiently apply axially symmetric DKI to even smaller data sets than those obtained with the 199 protocol. For example, as little as four directions with at least two non-vanishing b values may be sufficient to determine all parameters.

The second approach towards fast estimation of radial and axial kurtosis presented herein is somewhat less general, and requires the principal axis to be known beforehand, such that it may be chosen to coincide with one of the directions of the 199 protocol. This prerequisite could apply for spinal cord imaging, peripheral nerve imaging, or, for example, it could be fulfilled by fast acquisitions of the diffusion tensor followed by an alignment of the 199 protocol with the fiber of interest. Then axial kurtosis can be determined from two diffusion

weighted images acquired along the known principal diffusion axis at two b-values, in addition to the b=0 image. Radial kurtosis likewise requires two nonzero b-values, although in this case 4 distinct directions are necessary on each shell. In contrast to axially symmetric DKI, this method involves very simple post-processing, in particular no fitting is required. However, if conventional radial kurtosis should be estimated, it is necessary to fit the data in order to estimate all three diffusion tensor eigenvalues (unless axial symmetry is further assumed). This is built into our freely available Matlab scripts. The direct 199 approach was validated in the rat spinal cord, where most of the white matter has a fairly uniform primary diffusion eigenvector parallel to the spinal cord axis. The resulting parameter estimates were a bit noisier than their counterparts based on the full data set, but had similar overall contrast. The overall correlation was above 0.86 for all parameters, and the estimate of $K_{||}$ was better in white matter than in gray matter, as expected.

The direct 199 approach was slightly less accurate than the axially symmetric DKI, which could be partly due to deviations between the actual and the assumed direction of the principal diffusion direction, which will inevitably occur in practice. Another advantage of axially symmetric DKI is its ability to completely account for the full b-matrices, which is important when imaging cross terms contribute significantly to the diffusion weighting. This is typically the case with stimulated echo sequences or on animal systems with strong gradients. However, these advantages have to be weighed against the substantially simpler and faster postprocessing of the direct 199, which can heuristically account for full b-matrices to some degree as shown in (Hansen et al., 2015).

Conclusions

We introduced two strategies for reducing data requirements for DKI, and which may in particular be used with the 199 protocol introduced previously to extract additional information. The first was axially symmetric DKI, which operates with diffusion and kurtosis tensors having axial symmetry, and reduces the total DKI number of parameters from 22 to 8. Axially symmetric DKI was demonstrated in human brain in vivo and fixed rat spinal cord, and shown to provide good estimates of radial, axial, and mean tensor kurtosis, with reduced data demands. We also note that, in principle, all DKI parameters may be derived from small data sets using axially symmetric DKI. The second method was an extension of a previously introduced method for mean tensor kurtosis estimation, and relies on a priori knowledge of the primary diffusion direction. Although this method displayed good agreement with metrics from full DKI, its performance was slightly poorer than axially symmetric DKI. Both methods significantly reduce the minimum number of necessary diffusion weighted images, enabling accelerated imaging of the three DKI metrics, as well as DTI metrics.

Acknowledgments

The authors were supported by the Danish Ministry of Science, Technology and Innovation's University Investment Grant (MINDLab). BH acknowledges support from NIH 1R01EB012874-01. SNJ acknowledges support from the Lundbeck Foundation R83-A7548 and Simon Fougner Hartmans Familiefond. The authors wish to thank Lippert's Foundation and Korning's Foundation for financial support. The 3T Magnetom Tim Trio was funded by a grant from the Danish Agency for Science, Technology and Innovation. The authors thank Dr. Daniel Nunes from Champalimaud Neuroscience Programme for extraction of the spinal cord specimen.

References

- Barmpoutis A, Hwang MS, Howland D, Forder JR, Vemuri BC. Regularized positive-definite fourth order tensor field estimation from DW-MRI. *Neuroimage*. 2009; 45:S153–S162. [PubMed: 19063978]
- Bester M, Jensen JH, Babb JS, Tabesh A, Miles L, Herbert J, Grossman RI, Inglese M. Non-Gaussian diffusion MRI of gray matter is associated with cognitive impairment in multiple sclerosis. *Mult Scler*. 2015; 21:935–944. [PubMed: 25392318]
- Cheung, MM.; Hui, ES.; Wu, EX. Comparison of Directional Diffusion Kurtoses and Diffusivities in EAE-induced Spinal Cord. *ISMRM*; Toronto, Canada: 2008. p. 3328
- Conklin CJ, Middleton DM, Alizadeh M, Finsterbusch J, Raunig DL, Faro SH, Shah P, Krisa L, Sinko R, Delalic JZ, Mulcahey MJ, Mohamed FB. Spatially selective 2D RF inner field of view (iFOV) diffusion kurtosis imaging (DKI) of the pediatric spinal cord. *NeuroImage : Clinical*. 2016; 11:61–67. [PubMed: 26909329]
- Fieremans E, Jensen JH, Helpers JA. White matter characterization with diffusional kurtosis imaging. *Neuroimage*. 2011; 58:177–188. [PubMed: 21699989]
- Flint JJ, Hansen B, Fey M, Schmidig D, King MA, Vestergaard-Poulsen P, Blackband SJ. Cellular-level diffusion tensor microscopy and fiber tracking in mammalian nervous tissue with direct histological correlation. *Neuroimage*. 2010; 52:556–561. [PubMed: 20403443]
- Ghosh A, Milne T, Deriche R. Constrained diffusion kurtosis imaging using ternary quartics & MLE. *Magnetic Resonance in Medicine*. 2014; 71:1581–1591. [PubMed: 23821241]
- Giannelli M, Toschi N. On the use of trace-weighted images in body diffusional kurtosis imaging. *Magnetic Resonance Imaging*. 2016; 34:502–507. [PubMed: 26706136]
- Glenn GR, Helpers JA, Tabesh A, Jensen JH. Quantitative assessment of diffusional kurtosis anisotropy. *NMR Biomed*. 2015; 28:448–459. [PubMed: 25728763]
- Golkov, V.; Dosovitskiy, A.; Sämann, P.; Sperl, JI.; Sprenger, T.; Czisch, M.; Menzel, MI.; Gómez, PA.; Haase, A.; Brox, T.; Cremers, D. q-Space Deep Learning for Twelve-Fold Shorter and Model-Free Diffusion MRI Scans. In: Navab, N.; Hornegger, J.; Wells, MW.; Frangi, FA., editors. *Proceedings, Part I; Medical Image Computing and Computer-Assisted Intervention -- MICCAI 2015: 18th International Conference; Munich, Germany. October 5–9, 2015*; Cham: Springer International Publishing; 2015. p. 37-44.
- Grossman EJ, Ge Y, Jensen JH, Babb JS, Miles L, Reaume J, Silver JM, Grossman RI, Inglese M. Thalamus and cognitive impairment in mild traumatic brain injury: a diffusional kurtosis imaging study. *J Neurotrauma*. 2012; 29:2318–2327. [PubMed: 21639753]
- Guglielmetti C, Veraart J, Roelant E, Mai Z, Daans J, Van Audekerke J, Naeyaert M, Vanhoutte G, Delgado YPR, Praet J, Fieremans E, Ponsaerts P, Sijbers J, Van der Linden A, Verhoye M. Diffusion kurtosis imaging probes cortical alterations and white matter pathology following cuprizone induced demyelination and spontaneous remyelination. *Neuroimage*. 2016; 125:363–377. [PubMed: 26525654]
- Hansen B, Flint JJ, Heon-Lee C, Fey M, Vincent F, King MA, Vestergaard-Poulsen P, Blackband SJ. Diffusion tensor microscopy in human nervous tissue with quantitative correlation based on direct histological comparison. *Neuroimage*. 2011; 57:1458–1465. [PubMed: 21575730]
- Hansen, B.; Jespersen, SN. Scientific reports. 2016. Kurtosis fractional anisotropy, its contrast and estimation by proxy. In press
- Hansen B, Lund TE, Sangill R, Jespersen SN. Experimentally and computationally fast method for estimation of a mean kurtosis. *Magn Reson Med*. 2013a; 69:1754–1760. [PubMed: 23589312]
- Hansen B, Lund TE, Sangill R, Jespersen SN. Erratum: Hansen, Lund, Sangill, and Jespersen. Experimentally and Computationally Fast Method for Estimation of a Mean Kurtosis Magnetic Resonance in Medicine. 2014a; 69:1754–1760. *Magnetic Resonance in Medicine*. 2013; 71:2250–2250.
- Hansen B, Lund TE, Sangill R, Stubbe E, Finsterbusch J, Jespersen SN. Experimental considerations for fast kurtosis imaging. *Magn Reson Med*. 2015

- Hansen, B.; Sangill, R.; Lund, TE.; Jespersen, SN. A fast and robust method for simultaneous estimation of mean diffusivity and mean tensor kurtosis. *Proc. Int. Soc. Magn. Reson. Med; Milan, Italy.* 2014b. p. 4366
- Hansen MB, Jespersen SN, Leigland LA, Kroenke CD. Using diffusion anisotropy to characterize neuronal morphology in gray matter: the orientation distribution of axons and dendrites in the NeuroMorpho. org database *Front Integr Neurosci.* 2013b; 7:31. [PubMed: 23675327]
- Hardin RH, Sloane NJA. McLaren's improved snub cube and other new spherical designs in three dimensions. *Discrete & Computational Geometry.* 1996; 15:429–441.
- Hui ES, Cheung MM, Qi L, Wu EX. Advanced MR diffusion characterization of neural tissue using directional diffusion kurtosis analysis. *Conf Proc IEEE Eng Med Biol Soc.* 2008a; 2008:3941–3944. [PubMed: 19163575]
- Hui ES, Cheung MM, Qi L, Wu EX. Towards better MR characterization of neural tissues using directional diffusion kurtosis analysis. *Neuroimage.* 2008b; 42:122–134. [PubMed: 18524628]
- Jensen JH, Helpen JA. MRI quantification of non-Gaussian water diffusion by kurtosis analysis. *NMR Biomed.* 2010; 23:698–710. [PubMed: 20632416]
- Jensen JH, Helpen JA, Ramani A, Lu H, Kaczynski K. Diffusional kurtosis imaging: the quantification of non-gaussian water diffusion by means of magnetic resonance imaging. *Magn Reson Med.* 2005; 53:1432–1440. [PubMed: 15906300]
- Jespersen SN. Equivalence of double and single wave vector diffusion contrast at low diffusion weighting. *NMR Biomed.* 2012; 25:813–818. [PubMed: 22134913]
- Jespersen SN, Bjarkam CR, Nyengaard JR, Chakravarty MM, Hansen B, Vosegaard T, Ostergaard L, Yablonskiy D, Nielsen NC, Vestergaard-Poulsen P. Neurite density from magnetic resonance diffusion measurements at ultrahigh field: comparison with light microscopy and electron microscopy. *Neuroimage.* 2010; 49:205–216. [PubMed: 19732836]
- Jespersen SN, Kroenke CD, Ostergaard L, Ackerman JJ, Yablonskiy DA. Modeling dendrite density from magnetic resonance diffusion measurements. *Neuroimage.* 2007; 34:1473–1486. [PubMed: 17188901]
- Jones DK, Knosche TR, Turner R. White matter integrity, fiber count, and other fallacies: the do's and don'ts of diffusion MRI. *Neuroimage.* 2013; 73:239–254. [PubMed: 22846632]
- Kelm ND, West KL, Carson RP, Gochberg DF, Ess KC, Does MD. Evaluation of diffusion kurtosis imaging in ex vivo hypomyelinated mouse brains. *Neuroimage.* 2016; 124:612–626. [PubMed: 26400013]
- Kiselev, VG. The Cumulant Expansion: An Overarching Mathematical Framework For Understanding Diffusion NMR. In: Jones, DK., editor. *Diffusion MRI : theory, methods, and applications.* Oxford University Press; 2011. p. 152-168.
- Neto Henriques R, Correia MM, Nunes RG, Ferreira HA. Exploring the 3D geometry of the diffusion kurtosis tensor--impact on the development of robust tractography procedures and novel biomarkers. *Neuroimage.* 2015; 111:85–99. [PubMed: 25676915]
- Nie X, Hamlett ED, Granholm AC, Hui ES, Helpen JA, Jensen JH, Boger HA, Collins HR, Falangola MF. Evidence of altered age-related brain cytoarchitecture in mouse models of down syndrome: a diffusional kurtosis imaging study. *Magn Reson Imaging.* 2015; 33:437–447. [PubMed: 25527393]
- Ostergaard L, Engedal TS, Aamand R, Mikkelsen R, Iversen NK, Anzabi M, Naess-Schmidt ET, Drasbek KR, Bay V, Blicher JU, Tietze A, Mikkelsen IK, Hansen B, Jespersen SN, Juul N, Sorensen JC, Rasmussen M. Capillary transit time heterogeneity and flow-metabolism coupling after traumatic brain injury. *J Cereb Blood Flow Metab.* 2014; 34:1585–1598. [PubMed: 25052556]
- Poot DH, den Dekker AJ, Achten E, Verhoye M, Sijbers J. Optimal experimental design for diffusion kurtosis imaging. *IEEE Trans Med Imaging.* 2010; 29:819–829. [PubMed: 20199917]
- Qi LQ, Han DR, Wu EX. Principal invariants and inherent parameters of diffusion kurtosis tensors. *Journal of Mathematical Analysis and Applications.* 2009; 349:165–180.
- Qi LQ, Wang YJ, Wu EX. D-eigenvalues of diffusion kurtosis tensors. *Journal of Computational and Applied Mathematics.* 2008; 221:150–157.
- Rudrapatna SU, Wieloch T, Beirup K, Ruscher K, Mol W, Yanev P, Leemans A, van der Toorn A, Dijkhuizen RM. Can diffusion kurtosis imaging improve the sensitivity and specificity of detecting

- microstructural alterations in brain tissue chronically after experimental stroke? Comparisons with diffusion tensor imaging and histology *Neuroimage*. 2014; 97:363–373. [PubMed: 24742916]
- Sun PZ, Wang Y, Mandeville E, Chan ST, Lo EH, Ji X. Validation of fast diffusion kurtosis MRI for imaging acute ischemia in a rodent model of stroke. *NMR Biomed*. 2014; 27:1413–1418. [PubMed: 25208309]
- Tabesh A, Jensen JH, Ardekani BA, Helpert JA. Estimation of tensors and tensor-derived measures in diffusional kurtosis imaging. *Magn Reson Med*. 2011; 65:823–836. [PubMed: 21337412]
- Tachibana Y, Obata T, Tsuchiya H, Omatsu T, Kishimoto R, Kawaguchi H, Nishikori A, Kamagata K, Hori M, Aoki S, Tsuji H, Inoue T. Diffusion-tensor-based method for robust and practical estimation of axial and radial diffusional kurtosis. *Eur Radiol*. 2015
- Tietze A, Hansen MB, Ostergaard L, Jespersen SN, Sangill R, Lund TE, Geneser M, Hjelm M, Hansen B. Mean Diffusional Kurtosis in Patients with Glioma: Initial Results with a Fast Imaging Method in a Clinical Setting. *AJNR Am J Neuroradiol*. 2015; 36:1472–1478. [PubMed: 25977481]
- Veraart J, Van Hecke W, Sijbers J. Constrained maximum likelihood estimation of the diffusion kurtosis tensor using a Rician noise model. *Magn Reson Med*. 2011; 66:678–686. [PubMed: 21416503]
- Weber RA, Hui ES, Jensen JH, Nie X, Falangola MF, Helpert JA, Adkins DL. Diffusional kurtosis and diffusion tensor imaging reveal different time-sensitive stroke-induced microstructural changes. *Stroke*. 2015; 46:545–550. [PubMed: 25563646]
- Westin CF, Maier SE, Mamata H, Nabavi A, Jolesz FA, Kikinis R. Processing and visualization for diffusion tensor MRI. *Med Image Anal*. 2002; 6:93–108. [PubMed: 12044998]
- Wu Y, Kim J, Chan S-T, Zhou IY, Guo Y, Igarashi T, Zheng H, Guo G, Sun PZ. Comparison of image sensitivity between conventional tensor-based and fast diffusion kurtosis imaging protocols in a rodent model of acute ischemic stroke. *NMR in Biomedicine*. 2016a n/a–n/a.
- Wu Y, Kim J, Chan ST, Zhou IY, Guo Y, Igarashi T, Zheng H, Guo G, Sun PZ. Comparison of image sensitivity between conventional tensor-based and fast diffusion kurtosis imaging protocols in a rodent model of acute ischemic stroke. *NMR Biomed*. 2016b; 29:625–630. [PubMed: 26918411]

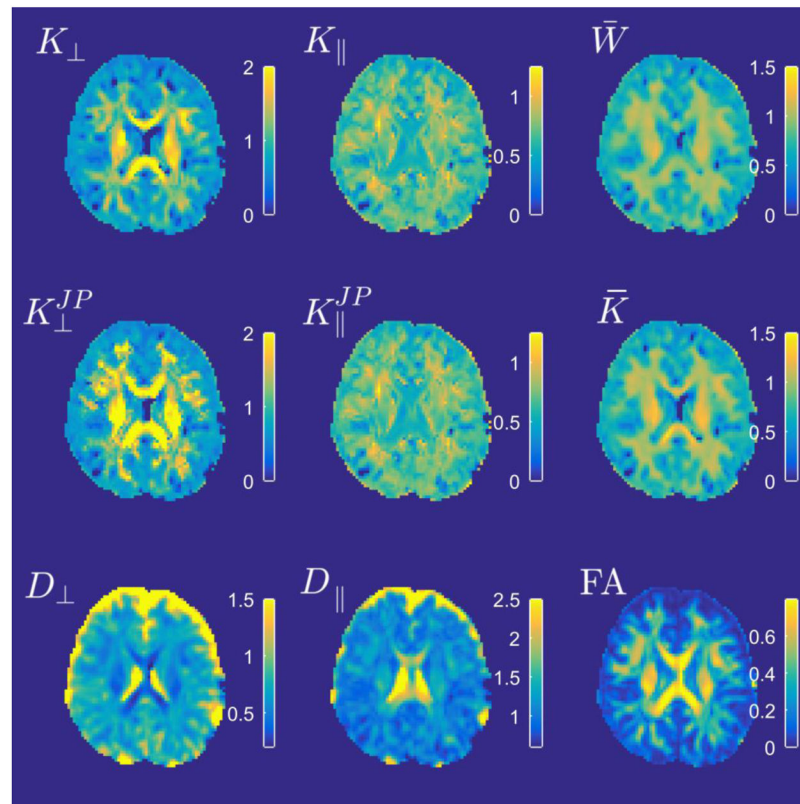


Figure 1.

The top row shows the proposed radial and axial kurtosis and MKT (i.e. \bar{W}) (from left to right) in human brain. The conventionally defined counterparts are shown in the middle row. Radial and axial diffusivities, along with FA, are also shown for comparison (left to right, bottom row). Diffusivities are given in units of $\mu\text{m}^2/\text{ms}$.

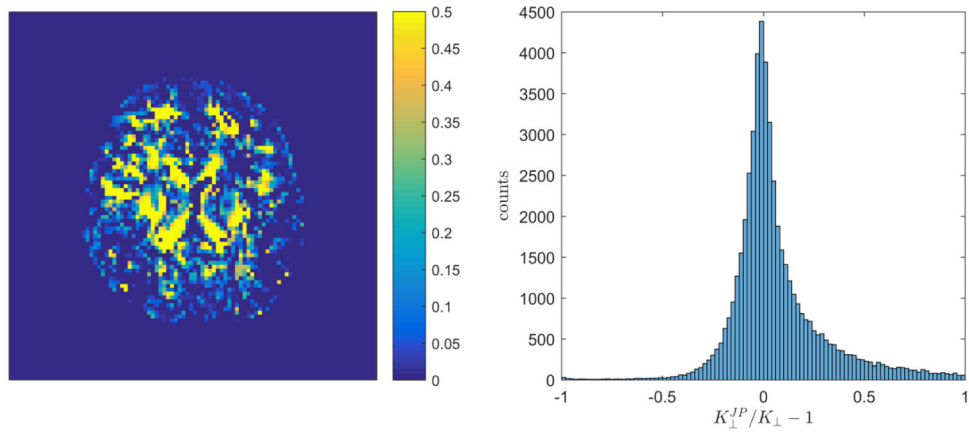


Figure 2.

The map on the left shows the relative difference between the Jensen/Poot definition (K_{\perp}^{JP}) and our K_{\perp} . The corresponding histogram is shown on the right. The figure is based on the same data used as in Fig. 1.

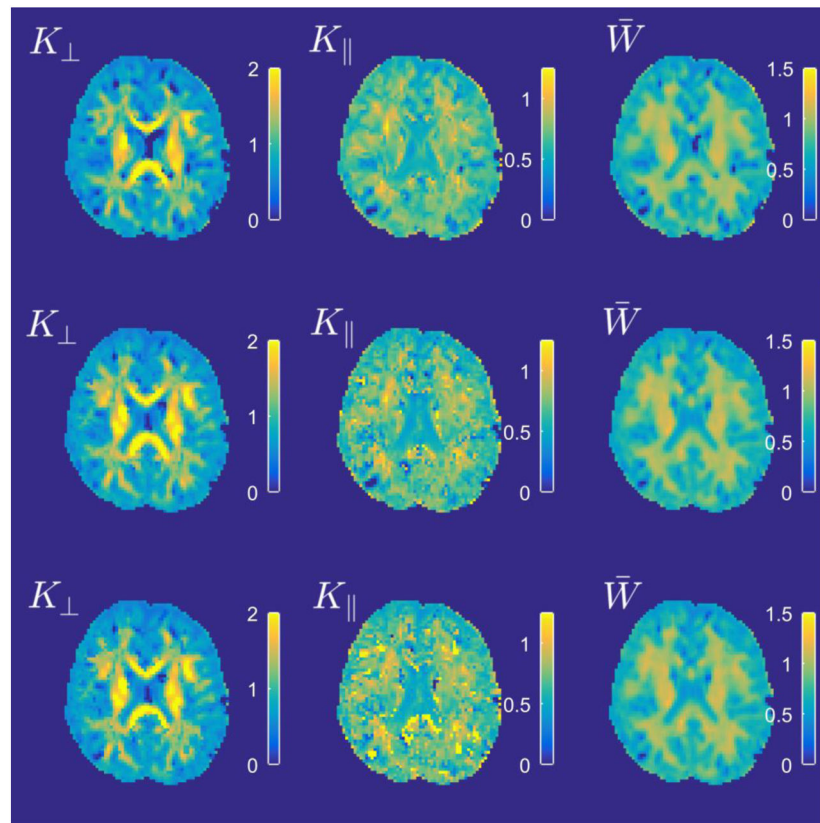


Figure 3.

Comparison of radial, axial, and mean kurtosis (left to right) obtained from a general DKI fit (top row) to those obtained from a DKI fit assuming axially symmetric kurtosis and diffusion tensors (middle row). Here the full data set was used in the estimation. The bottom row shows the parameter estimates obtained when fitting the axially symmetric model to a 199 subset of the data.

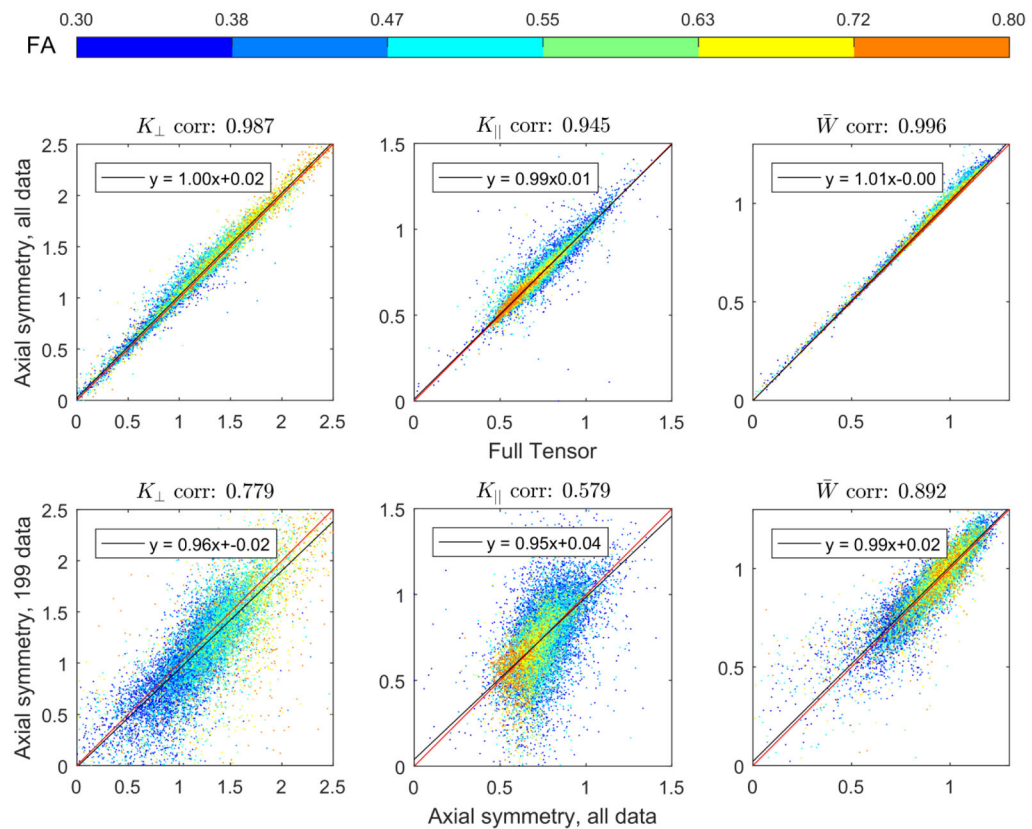


Figure 4.

Scatterplots comparing radial, axial, and mean tensor kurtosis over all 22 slices in the human data set. Data points are color coded according to their FA values. The top panel compares full tensor metrics to analogous metrics obtained from axially symmetric DKI. The bottom panel compares axially symmetric DKI obtained using all diffusion weighted images to those obtained using only a subset corresponding to 199 data. Less than 4% of the data fall outside the shown ranges. In each plot, the red line is the identity line and the black line is the best straight line fit (robustfit) to the data.

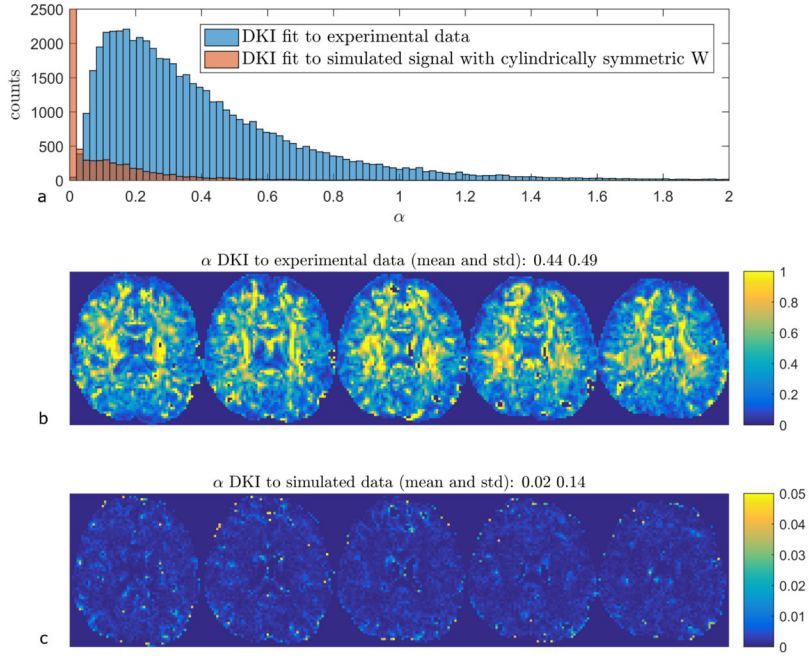


Figure 5. Demonstration of variability in equatorial kurtosis for the full DKI fitted to actual data and to data synthesized from the axially symmetric fit (equal data sizes and with noise added in quadrature to match the experimental SNR = 39 at b=0). Panel a) shows histograms of $\alpha = (W_{\max} - W_{\min})/W_{\perp}$ for both fits (whole brain). The count in the first bin from the simulated signal is ~50,000. Panel b) provides maps of α in five consecutive slices from the fit to actual data. Similarly, panel c) shows α from the fit to synthetic axially symmetric data.

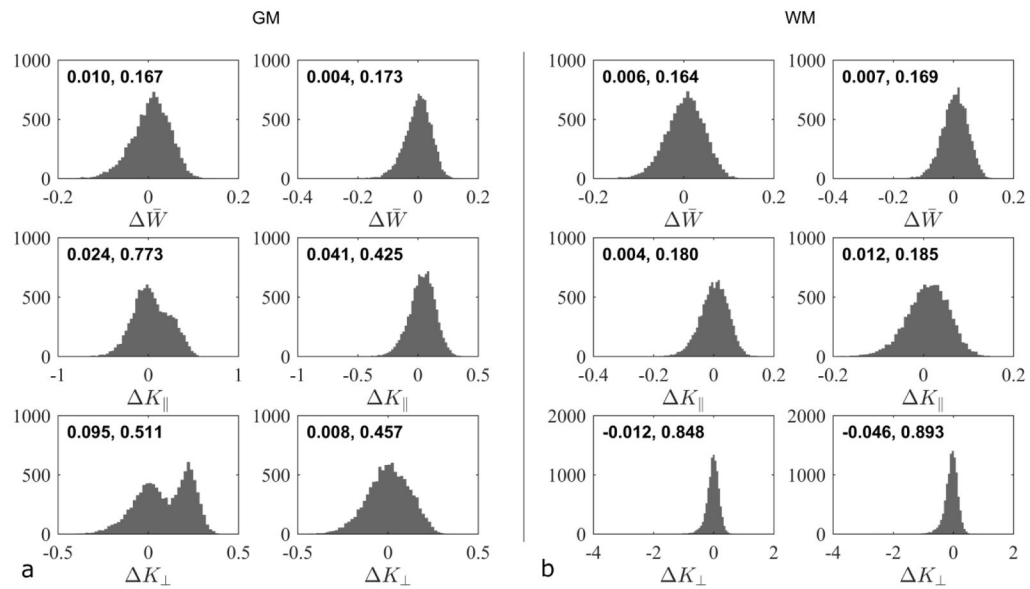


Figure 6. histograms of estimated kurtosis metrics errors from a) a white matter voxel ($\bar{W}= 1.07$, $FA= 0.78$, $\alpha= 0.28$) and b) a gray matter voxel ($\bar{W}= 0.79$, $FA= 0.12$, $\alpha = 0.36$). In each panel, the left column shows metrics estimated with axially symmetric DKI, whereas the right column estimates are based on the unconstrained conventional DKI. The data were generated numerically by computing the signal using full diffusion and kurtosis tensors estimated from the corresponding voxels in the full human brain data set with unconstrained DKI. Rician noise was then added to match the experimental SNR of 39, and axially symmetric DKI as well as unconstrained DKI was then fitted to the noisy signal. This process was repeated 1000 times. Numbers inside each graph frame are median and mid-95% range.

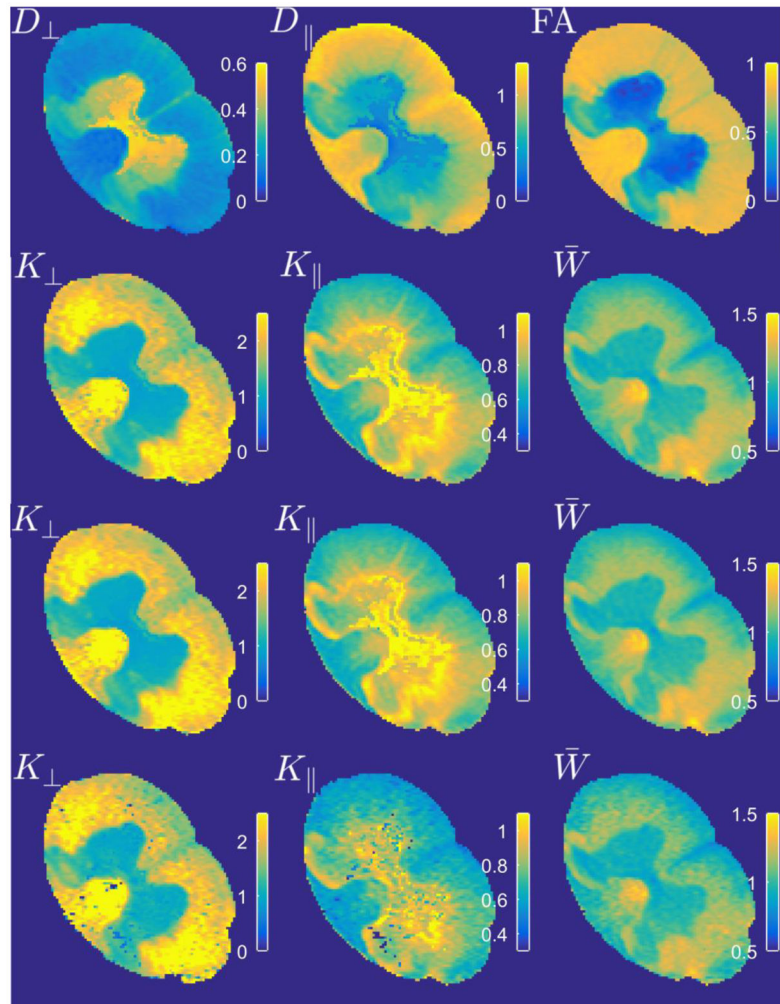


Figure 7. Same as Fig. 3, but for the rat spinal cord data. Top row (left to right): Comparison of radial and axial diffusivity ($\mu\text{m}^2/\text{ms}$), and FA. In the lower panels, radial, axial, and mean kurtosis obtained from a general DKI fit (second row) are compared to those obtained from a DKI fit assuming axially symmetric kurtosis and diffusion tensors using the entire data set (third row) and a 199 subset of the data (bottom row).

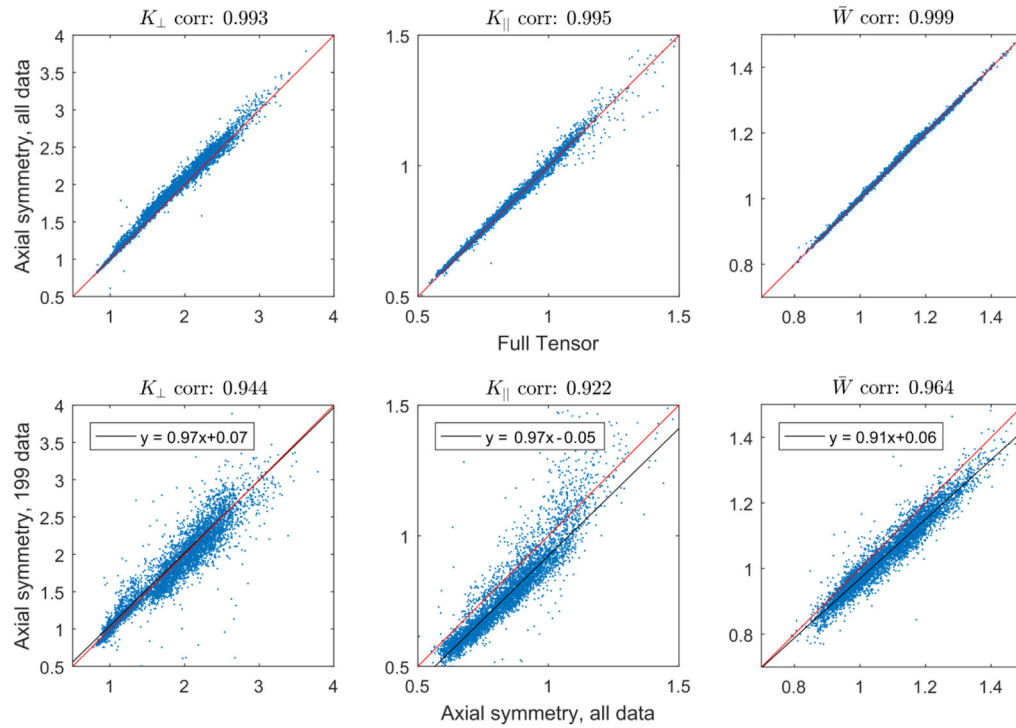


Figure 8.

Scatterplots comparing radial, axial, and MKT in the rat spinal cord. The top panel compares full tensor metrics to analogous metrics obtained from axially symmetric DKI, where less than 3% of the data fell outside of the range shown. The bottom panel compares axially symmetric DKI obtained using all diffusion weighted images to those obtained using only a subset corresponding to 199 data. Less than 1% of the data are outside of the shown ranges. In each plot, the red line is the identity line and (when present) the black line is the best straight line fit (robustfit) to the data.

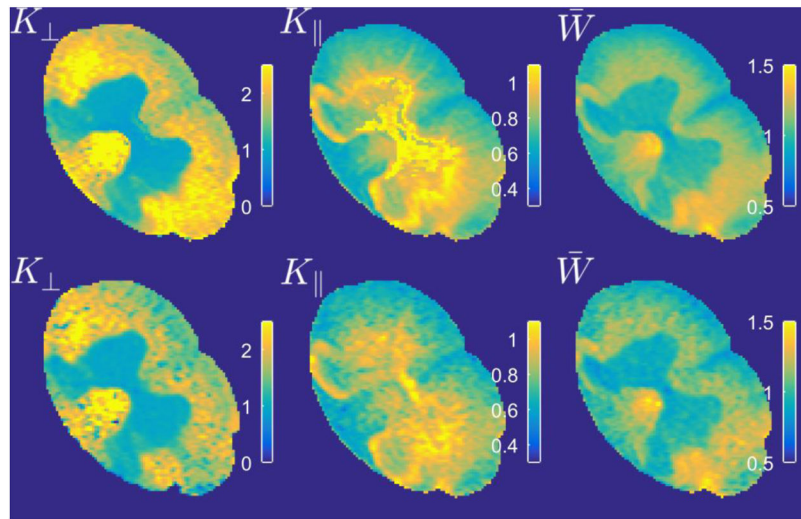


Figure 9. Maps of radial and axial kurtosis and MKT (left to right) from the direct 199 approach with assumed known principal diffusion direction (bottom row). For convenience, the top row shows the same maps from the nonlinear least squares estimation using the full data set.

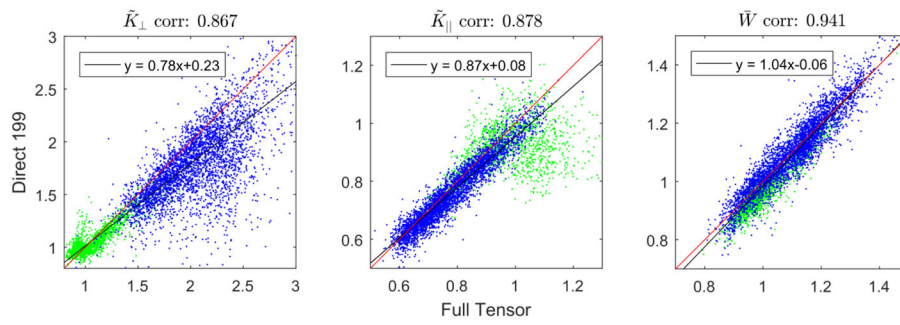


Figure 10.

Scatterplots corresponding to Fig. 9. Points in gray matter are in green, points in white matter are in blue. At most 2% of the data fall outside the shown ranges. In each plot, the red line is the identity line and the black line is the best straight line fit (robustfit) to the data.

Table 1

The nine directions $\hat{n}^{(i)}$, $\hat{n}^{(i+)}$ and $\hat{n}^{(i-)}$, $i=1,2,3$.

Direction	x	y	z
n^1	1	0	0
n^{1+}	0	$1/\sqrt{2}$	$1/\sqrt{2}$
n^{1-}	0	$1/\sqrt{2}$	$-1/\sqrt{2}$
n^2	0	1	0
n^{2+}	$1/\sqrt{2}$	0	$1/\sqrt{2}$
n^{2-}	$1/\sqrt{2}$	0	$-1/\sqrt{2}$
n^3	0	0	1
n^{3+}	$1/\sqrt{2}$	$1/\sqrt{2}$	0
n^{3-}	$1/\sqrt{2}$	$-1/\sqrt{2}$	0